ASIA-PACIFIC SOLAR RESEARCH CONFERENCE

2016

Peer Reviewed
2016 Solar Research Conference

Thermal Elastic Stress in Sodium Receiver Tubes

William R. Logie, John D. Pye and Joe Coventry

Solar Thermal Group, Research School of Engineering, Australian National University
E-mail: will.logie@anu.edu.au

Abstract

Linear-elastic stress in nonaxisymmetrically heated receiver tubes is calculated with analytical equations from Timoshenko & Goodier (1951) and compared against results from a Finite Volume Method (FVM) OpenFOAM® model. Principal component and equivalent stress is shown for receiver tubes carrying molten salt and liquid sodium. It is found that compressive front-side axial stress is the largest component in equivalent tube stress. Sensitivity of stress to internal convection coefficient, tube size, tube conductivity and tube internal pressure is explored.

1 Introduction

Tubes are used extensively on high temperature solar receivers because they are good pressure vessels, the flow within them is well understood and individual tubes are allowed to thermally deform independently of one another in reponse to locally-varying flux. Optimisation of tubes for a specific fluid and receiver configuration requires an accurate understanding of loss mechanisms - radiation, convection, conduction and friction. Higher efficiency may be achieved by increasing temperature to the power block or by using liquid metals such as sodium to improve internal heat transfer and thereby decrease tube external surface temperatures and thus loss to environment (Pye *et al.* , 2014, Logie *et al.* , 2015, Coventry *et al.* , 2016).

For indirectly heated fluid receivers, thermally induced stress in the containment material (e.g. nickel-chromium alloy) becomes a key constraint on the allowable receiver flux (Liao *et al.* , 2014, Kim *et al.* , 2016). This work compares the analytical methods from Timoshenko & Goodier (1951) with numerical results obtained using a Finite Volume Method (FVM) OpenFOAM® linear-elastic thermal stress solver (Tuković *et al.* , 2014), making use of the *equivalent* or *von Mises* stress:

$$\sigma_{\mathrm{Eq}} = \sqrt{\frac{1}{2}\left[(\sigma_1-\sigma_2)^2+(\sigma_2-\sigma_3)^2+(\sigma_3-\sigma_1)^2\right]}, \tag{1}$$

where indexes refer to the cylindrical (r, θ, z) or Cartesian (x, y, z) coordinate system[1]. Assumption of constrained and unconstrained tube ends is illustrated with case 135 (p412) from Timoshenko & Goodier.

[1]Sometimes principal stress components are converted for comparison

The sensitivity of maximum equivalent stress is explored for tubes carrying molten salt and liquid sodium over a range of typical receiver tube parameters in a manner similar to Logie *et al.* (2015).

2 Laplacian-Fourier $\mathscr{L}$-$\mathscr{F}$ Python Model

The approach to modelling a receiver tube is to consider it as a series of finite cylindrical segments with inner radius a and outer radius b where the temperature is assumed to vary in the radial r and angular coordinate θ but not axially z. It is also assumed that the temperature distribution reaches its steady-state and can be found by way of the Laplace equation in cylindrical coordinates:

$$\nabla^2 T = 0 \tag{2}$$

$$\frac{\partial^2 T}{\partial r^2} + \frac{1}{r}\frac{\partial T}{\partial r} + \frac{1}{r^2}\frac{\partial^2 T}{\partial \theta^2} = 0. \tag{3}$$

For trivial boundary conditions (i.e. specified temperature or heat flux) the *separation of variables* or Fourier method can provide solutions to such two or three dimensional steady-state problems algebraically, however where *mixed boundary conditions* are to be implemented solutions using this mathematical tool are not easy to obtain (Hetnarski & Eslami, 2009). For this reason the Gauss-Seidel *iterative* method was implemented in Python (Kiusalaas, 2010) on a half cylindrical coordinate system ($0 < \theta < 180°$) as illustrated in Figure 1 to obtain the steady-state temperature field.

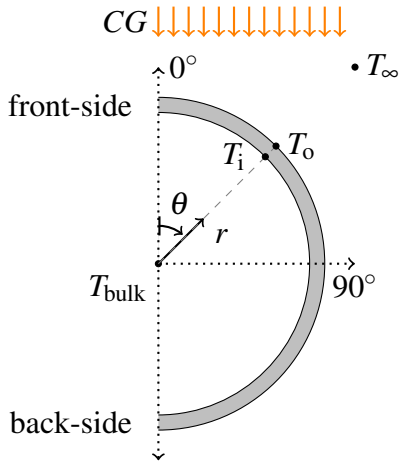

Figure 1: Laplacian model notation

Neumann boundary conditions are applied reflecting the absorption of collimated flux, reradiation and convection to environment:

$$k\left.\frac{\partial T}{\partial r}\right|_{r=b} = \left\{\begin{array}{ll} \alpha_{rad} CG\cos(\theta) & : 0 \le \theta \le 90° \\ 0 & : \text{otherwise} \end{array}\right\} - \varepsilon_{rad}\sigma_{rad}(T_o^4 - T_\infty^4) - h_o(T_o - T_\infty), \tag{4}$$

and forced convection to molten salt or liquid sodium:

$$k\left.\frac{\partial T}{\partial r}\right|_{r=a} = h_i(T_{bulk} - T_i), \tag{5}$$

where k is tube conductivity, $\alpha_{\text{rad}} = 0.97$ and $\varepsilon_{\text{rad}} = 0.87$ is Pyromark® absorptivity and emissivity respectively, CG is the solar concentration ratio constant, σ_{rad} is the Stefan-Boltzmann constant and h is convection coefficient of either inside or outside tube surface (subscripts i and o respectively). A further description of their determination is found in Pye *et al.* (2014) and in regards to their implementation in the OpenFOAM® model in Logie *et al.* (2015).

With two-dimensional steady-state heat flow established, the principal thermal elastic stress components σ_r and σ_θ may be found by superposition of axisymmetrical and nonaxisymmetrical parts. Two slightly differing approaches based on the same biharmonic theory exist in established literature (Irfan & Chapman, 2009, Marugán-Cruz *et al.* , 2016), namely that from Timoshenko & Goodier (1951) and that from Gatewood (1941). In both approaches the axisymmetrical parts for σ_r and σ_θ can be found with:

$$\sigma_r = \frac{E\alpha(\overline{T}_\text{i} - \overline{T}_\text{o})}{2(1-\nu)\log\frac{b}{a}}\left[-\log\frac{b}{r} - \frac{a^2}{b^2-a^2}\left(1-\frac{b^2}{r^2}\right)\log\frac{b}{a}\right] \tag{6}$$

$$\sigma_\theta = \frac{E\alpha(\overline{T}_\text{i} - \overline{T}_\text{o})}{2(1-\nu)\log\frac{b}{a}}\left[1-\log\frac{b}{r} - \frac{a^2}{b^2-a^2}\left(1+\frac{b^2}{r^2}\right)\log\frac{b}{a}\right] \tag{7}$$

where E is the tube's modulus of elasticity, α is its linear coefficient of thermal expansion, ν is Poisson's ratio, and mean surface temperatures:

$$\overline{T}_\text{i} = \frac{1}{2\pi}\int_0^{2\pi} T_\text{i}\,\mathrm{d}\theta, \qquad \overline{T}_\text{o} = \frac{1}{2\pi}\int_0^{2\pi} T_\text{o}\,\mathrm{d}\theta, \tag{8}$$

are shown here for a complete circumference 2π. In the Timoshenko & Goodier approach the nonaxisymmetrical parts are handled with inside and outside cylinder temperatures as functions of the angular coordinate θ only, the coefficients for which are determined here with a non-linear least-squares fitting algorithm[2] for respective Fourier functions:

$$T_\text{i} = \overline{T}_\text{i} + A_1\cos\theta + A_2\cos 2\theta + \cdots + A_1'\sin\theta + A_2'\sin 2\theta + \cdots \tag{9}$$

$$T_\text{o} = \overline{T}_\text{o} + B_1\cos\theta + B_2\cos 2\theta + \cdots + B_1'\sin\theta + B_2'\sin 2\theta + \cdots \tag{10}$$

as illustrated in Figure 2 with four terms.

The net heat flow from outside to inside corresponding to terms $\cos 2\theta$, $\sin 2\theta$ and greater is zero, thus the only mild stress they produce is in the axial direction. Owing to the terms $A_1\cos\theta$ and $B_1\cos\theta$ there are stress components:

$$\sigma_r = \kappa\cos\theta r\left(1-\frac{a^2}{r^2}\right)\left(\frac{b^2}{r^2}-1\right) \tag{11}$$

$$\sigma_\theta = \kappa\cos\theta r\left(\frac{a^2b^2}{r^4} + \frac{a^2+b^2}{r^2} - 3\right) \tag{12}$$

where:

$$\kappa = -\frac{E\alpha}{2(1-\nu)}\left(\frac{A_1}{a} - \frac{B_1}{b}\right)\frac{a^2b^2}{b^2-a^2}. \tag{13}$$

[2] https://docs.scipy.org/doc/scipy-0.13.0/reference/generated/scipy.optimize.curve_fit.html

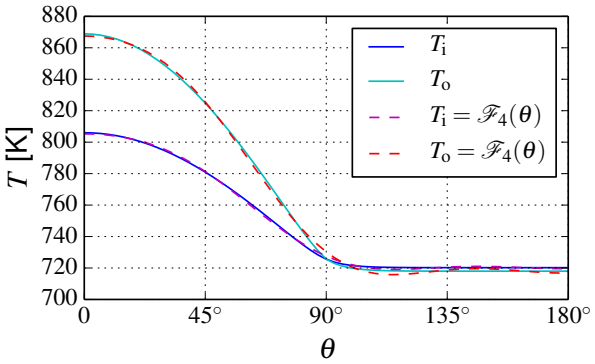

Figure 2: Temperatures of the Laplacian solution (solid) from Eq. 3 and their Fourier *fits* (dashed) from Eqns. 9 and 10

To determine the axial component of stress σ_z Timoshenko & Goodier assume zero axial displacement (plain-strain) and then modify the solution to reflect free ends by introducing an axial stress applied at the ends and opposite in sign to the plain-strain component such that the net axial force is zero. By St. Venant's principle the self-equilibrating distribution at the ends is ignored and a solution is given for a cross section far from them:

$$\sigma_z = -E\alpha(T - T_{\text{avg}}) + \left[2\kappa\nu\left(\frac{a^2+b^2}{r^2} - 2\right) + \kappa'\right] r\cos\theta \tag{14}$$

where:

$$\kappa' = E\alpha\left(\frac{B_1 b - A_1 a}{b^2 - a^2}\right) \tag{15}$$

In the Gatewood approach cylinder temperature is expressed as a single function of r and θ. Kim *et al.* (2016) obtained a favourable comparison with hoop stress σ_θ results from Finite Element Analysis (FEA), however Gatewood and others citing him (Hetnarski & Eslami, 2009) only mention the equation of plain-strain (zero axial displacement) for axial stress σ_z.

3 Results

It is important to recognise the two types of thermal expansion occurring for us to understand what is being accounted for. Firstly, there is that associated with getting from night-time cold state up to operation or bulk fluid temperature. Secondly there is that which happens beyond this largely homogeneous change, the increase in tube temperatures above this established *stress free* operating temperature from the heating condition. While not insignificant in magnitude, the first change in temperature is considered to have already happened in the following analysis and is therefore not considered.

To provide validation for the $\mathscr{L}$-$\mathscr{F}$ Python model, the OpenFOAM® model from Logie *et al.* (2015) was extended to run in a linear-elastic thermal stress solver (Tuković *et al.* , 2014)[3] with either constrained or unconstrained axial boundary conditions.

[3] https://github.com/wyldckat/FluidStructureInteraction

3.1 Axisymmetrically heated tubes

As in case 135 from p412 Timoshenko & Goodier, a condition of heating is set up in a *cylinder with a concentric circular hole*[4] with a uniform inside temperature $T_\mathrm{i} = 0°\mathrm{C}$ and a uniform outside temperature $T_\mathrm{o} = 100°\mathrm{C}$. The temperature distribution is taken to be symmetrical about the axis and independent of axial coordinate z (axisymmetric). For added surety the axisymmetrical component stresses are calculated from an analytical radial temperature distribution:

$$T = T_\mathrm{i} + \left[(T_\mathrm{o} - T_\mathrm{i}) \frac{\log \frac{r}{a}}{\log \frac{b}{a}} \right]. \tag{16}$$

The OpenFOAM® model could be made axisymmetrically but for illustration purposes a quarter circumference was modelled. Figure 3 shows an exaggeration of the displacement in the quarter-tube OpenFOAM® model when the ends are completely unconstrained. This axial condition does not reflect that assumed in Timoshenko & Goodier (ends kept planar) but results in the same axial stress profile at a cross section far from the ends.

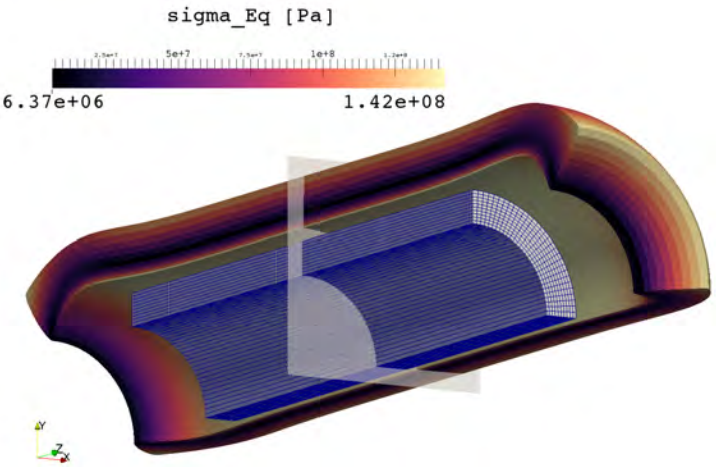

Figure 3: Cylinder with inside radius $a = 0.5$ m and outside radius $b = 0.7$ m; inner surface 0°C and outer surface 100°C; original mesh shown inside and a *warped* mesh $(u, v, w) \times 1000$ outside showing equivalent stress σ_Eq and the result of unconstrained ends.

Figure 4 shows component stress and a comparison of analytical equivalent stress against results sampled from the OpenFOAM® model. This served to validate the OpenFOAM® model and added confidence when implementing the analytical equations into the $\mathscr{L}$-$\mathscr{F}$ Python model, whose temperature solution was also validated against the analytical temperature distribution.

The assumption of constrained tube ends results in the largely compressive axial stress σ_z becoming the dominant component in the equivalent stress criterion σ_Eq (Figure 4a). The notion that axial stress can be ignored (Marugán-Cruz *et al.* , 2016, Kim *et al.* , 2016) possibly comes from the awareness that under the axisymmetrical heating condition unconstrained tubes have axial stress *more-or-less* equal in magnitude and character to hoop stress (Figure 4b).

If the thermal expansion of any increase in tube temperature above the bulk fluid's temperature was not allowed to happen then we would have a case of zero axial displacement, however

[4] One of the first *thermal stress* solutions ever published in 1838 by J. M. C Duhamel.

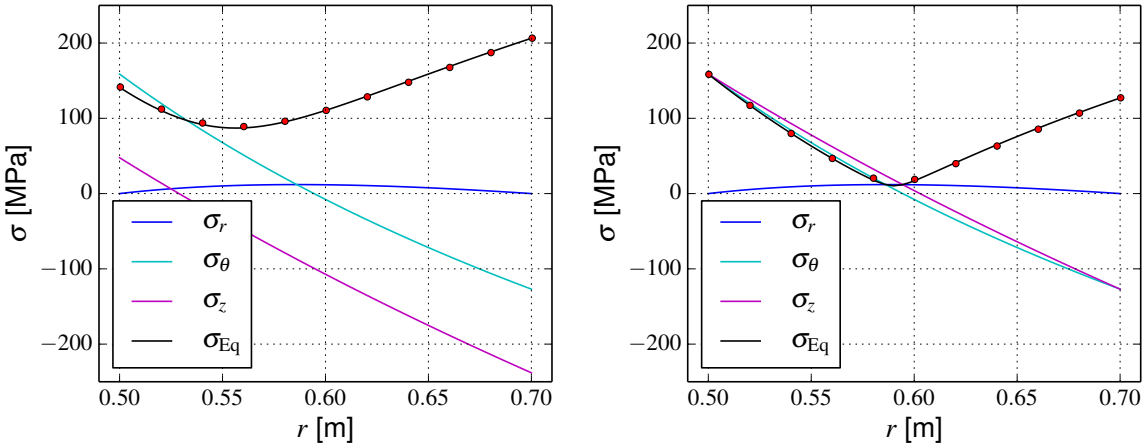

(a) Zero axial displacement

(b) Zero axial force

Figure 4: Timoshenko & Goodier (1951) case 135 (p412); sample of a component or equivalent stress through the tube material; solid lines denote results from $\mathscr{L}$-$\mathscr{F}$ Python model and coloured circles denote results sampled from the OpenFOAM® model; compression is negative and tension is positive

what we actually have is compression in the tube cross section where tube temperature is above the tube's average, and tension where tube temperature is below it. The resultant net axial stress is zero because the tension and compression balance out. The axial component of thermal stress (tube front-side to back-side temperature difference) is the most significant in the case of molten salt receiver tubes (Pacheco *et al.* , 1995) and can therefore be neither ignored nor incorrectly accounted for.

3.2 Nonaxisymmetrically heated tubes

In the following validation of the nonaxisymmetrical component stress model Schedule 5S tube is selected. It is available with a wall thickness of 1.65 mm in the nominal diameter range from DN15 up to DN50. A summary of the key fluid and flow properties for DN25 with a bulk fluid temperature 450°C is given in Table 1. The flow rates were chosen to reflect representative bulk tube velocities with a similar pressure drop.

Table 1: Exemplary tube flow properties evaluated at a bulk fluid temperature of 450°C for DN25 (1") Sch. 5S Haynes® 230 tubes

		Molten Salt	Liquid Sodium
Mass flow	kg/s	5	4
Bulk velocity	m/s	3.9	6.7
Reynolds Number	-	144,073	666,947
Pressure drop	kPa/m	−7.69	−7.85
Nusselt Number	-	548	19.6
Convection coefficient	kW/(m^{2}K)	9.7	43.6

Some careful consideration was needed when defining the axial boundary condition in the OpenFOAM® model (Figure 5). Axial stress arising from the thermal expansion of receiver tube panels is managed through the use of bellowed tube or bends with oblique attachment to the manifold, as shown by example in Figure 5b. Under a nonaxisymmetric heating condition the tube front-side is hotter than the back-side which remains roughly at the temperature of the heat transfer fluid (Figure 2). The tube cross section net axial stress is zero but there exists a *bending* stress with compression front-side and tension back-side. To capture this type of constraint in the OpenFOAM® model a one metre length of tube was constrained at one end with a fixed displacement BC and at the other with a mixed displacement/gradient BC; zero displacement in x and y coordinates and zero traction in the z coordinate. In addition the same mixed BC was also applied to short unheated cantilever-constraint end sections to keep symmetry and the cross section of the axially unconstrained tube end planar. The tube bows ever so slightly towards the heated side, as shown in Figure 5a - again with an exaggerated displacement in the mesh $(u, v, w) \times 1000$ - and while peak stress is observed at the transition zone between passive and bowed tube section, stress which would be indicative of that found in tubes between mounting supports of a panel is then sampled at a cross section midway between the ends.

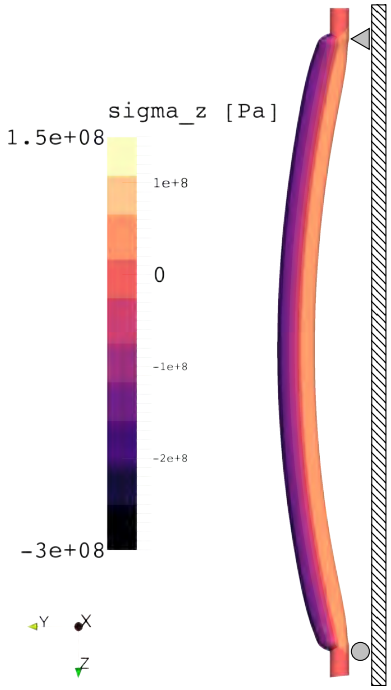

(a) σ_z of 1 m length of liquid sodium receiver tube irradiated with 800 kW/m^2 (from the left side); fixed axial BC top and free axial BC bottom; passive segments at either end not heated

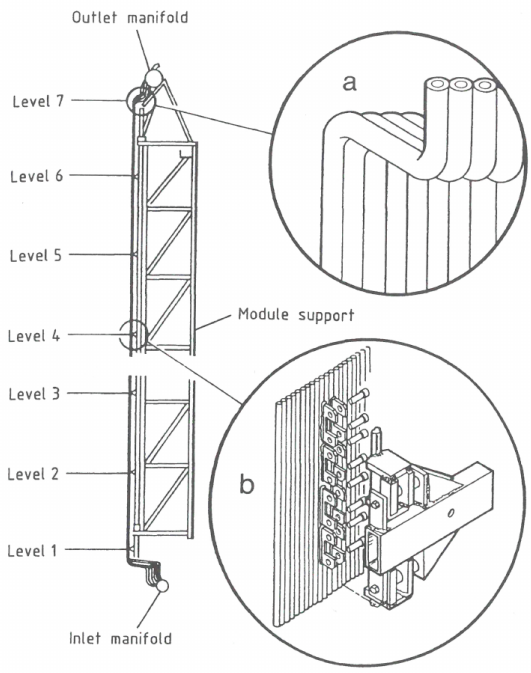

(b) Barstow *solar one* steam receiver details: stress relief bends on approach to manifold and mounting attachment to allow for thermal growth of panel (Winter *et al.* , 1991)

Figure 5: The *free* axial boundary condition

A complete set of component stress results from the $\mathscr{L}$-$\mathscr{F}$ Python model for the case of DN25 (1") tubes having flow properties for molten salt and liquid sodium defined as in Table 1 and irradiated with 800 kW/m^2 are shown in Figure 6. To help discern the magnitudes of stress Figure 7 shows each of the component stresses sampled through the tube wall at the front-side

so-called 0° Stress Classification Line (SCL) where, as in Figure 6c and 6f, it can be seen that the peak thermal stress is due to the hot front-side and thus largely compressive axial component of stress. A final set of figures incorporating all component stresses into the equivalent stress is given in Figure 8 in which the peak front-side stress in each case is annotated.

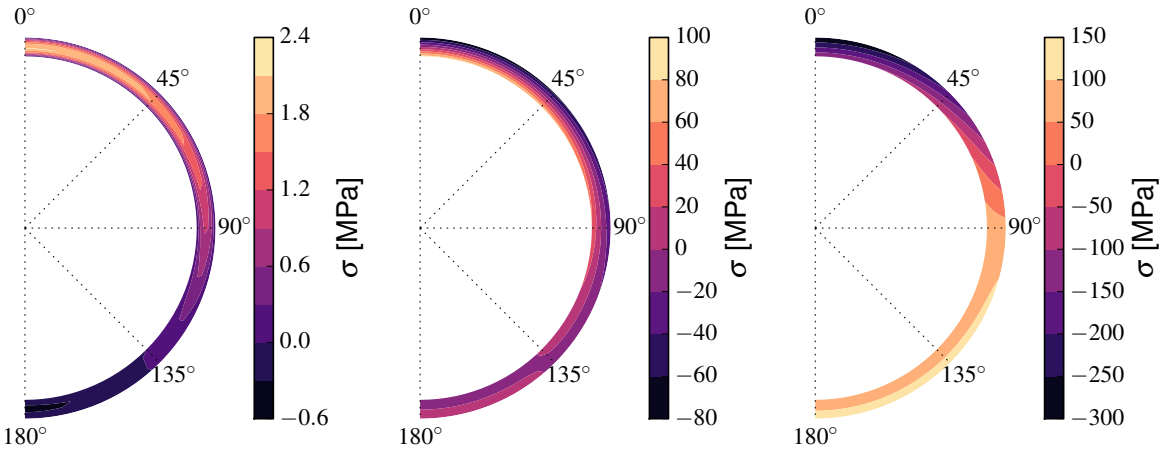

(a) Molten salt; σ_r **(b)** Molten salt; σ_θ **(c)** Molten salt; σ_z

(d) Liquid sodium: σ_r **(e)** Liquid sodium: σ_θ **(f)** Liquid sodium: σ_z

Figure 6: Component stress **(a)** - **(c)** for molten salt and **(d)** - **(f)** for liquid sodium generated with the $\mathscr{L}$-$\mathscr{F}$ Python model given an incident flux of 800 kW/m^2; compression is negative and tension is positive

One must look very close (e.g. zoom in on electronic version of document) when comparing Figure 6a and 6b with Figure 6d and 6e to discern a difference. Otherwise one might think them to be equal. What is to be observed is that maximum radial and circumferential stress is slightly higher in the case of liquid sodium than molten salt. The reason for this could be twofold. On the one hand losses to the environment (convection and radiation) in the case of liquid sodium tubes are less on account of the lower external tube temperature. The other possible reason is that heat is more orthogonally transferred to the fluid at the front-side of the tube which might result in a slightly *steeper* temperature gradient in the radial direction.

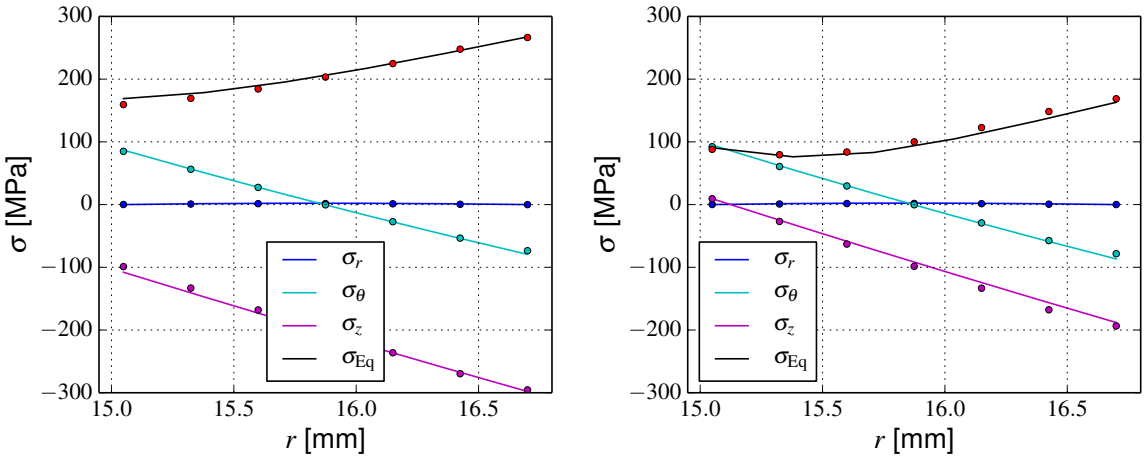

(a) Molten salt **(b)** Liquid sodium

Figure 7: Sample of component stresses along 0° Stress Classification Line (SCL); solid lines denote results from $\mathscr{L}$-$\mathscr{F}$ Python model and coloured circles denote results sampled from the OpenFOAM® model; compression is negative and tension is positive

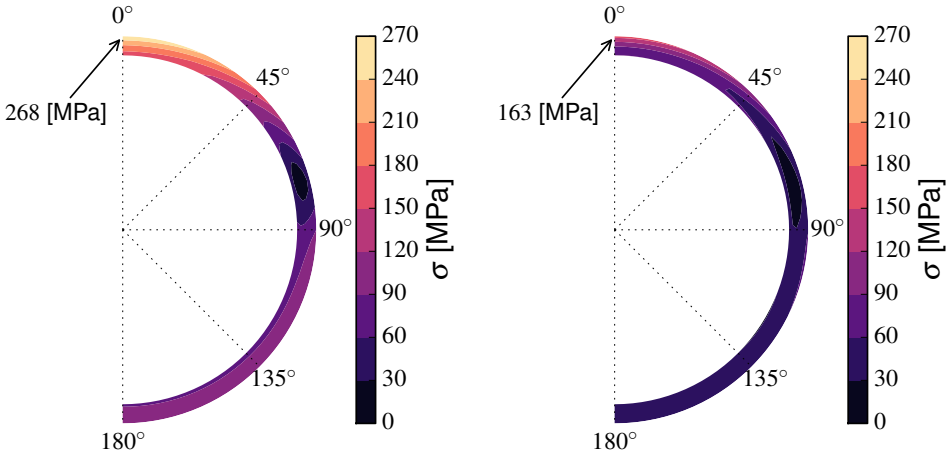

(a) Molten salt: σ_{Eq} **(b)** Liquid sodium: σ_{Eq}

Figure 8: Equivalent *von Mises* stress for tubes irradiated with 800 kW/m^2; peak stress at tube front-side annotated

Where the tubes with liquid sodium perform significantly better than those with molten salt is in regards to axial stress. Due to the lower overall front-side tube temperature, the *bending* stress over the tube's cross section is smaller, such that when observing the equivalent tube stress of liquid sodium versus molten salt in Figure 8, the difference between molten salt and liquid sodium peak tube stress is largely due to axial stress.

Allowing for modelling and discretisation error in the OpenFOAM® implementation, the agreement between OpenFOAM® and the $\mathscr{L}$-$\mathscr{F}$ Python model is quite good as observed with component stresses in Figure 7.

3.3 Parameter study

Some preliminary parameter studies were performed in which the analytical equations for pressure stress according to Timoshenko & Goodier are superposed on thermal stress. The parameters of internal convection coefficient, tube internal pressure, tube material conductivity and tube diameter were varied within an expected range for both liquid sodium and molten salt. The result on tube stress can be seen in Figure 9.

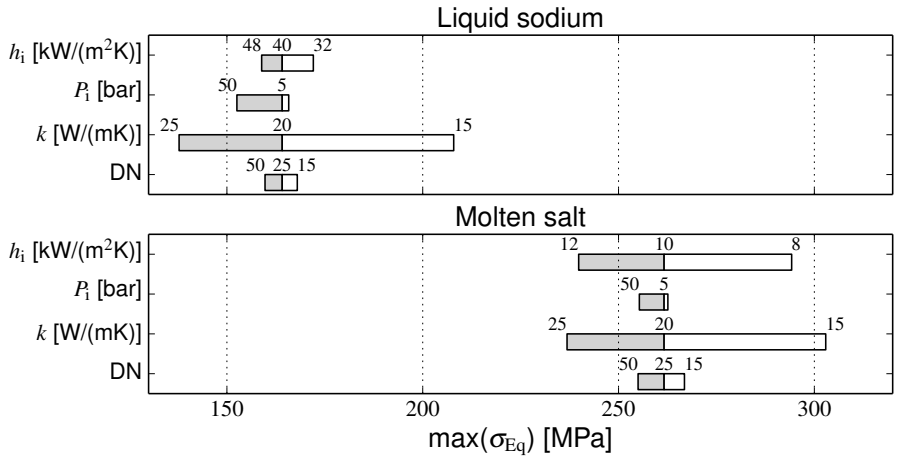

Figure 9: Sensitivity of maximum equivalent stress to internal convection coefficient, internal tube pressure, tube conductivity and tube diameter for liquid sodium and molten salt tubes irradiated with 800 kW/m^2

There is an inverse relationship between internal convection coefficient and maximum equivalent tube stress, and variations affecting the convection coefficient of molten salt are more strongly felt in tube stress than for the same change in convection coefficient of liquid sodium.

Owing to its non-linear tensile contribution to overall stress, the addition of pressure initially decreases equivalent stress, as can be seen more accurately in Figure 10. At some point the addition of more internal pressure results in tensile hoop stress dominating, although this point depends heavily on the original magnitude of compression due to thermal stress.

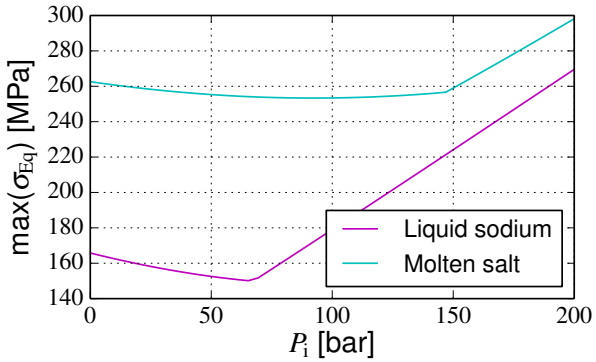

Figure 10: Impact of pressure on maximum equivalent tube stress; it is highly unlikely that such high pressures would be used in the case of molten salt and especially liquid sodium, given the danger of sodium spray fires

Tube conductivity decreases the temperature gradient for a given flux just as thinner tube wall reduces the temperature difference between outside and inside tube surfaces. More gradual temperature gradients result in lower stress. The choice of tube diameter impacts equivalent stress by changing the distance through which the bending moment in axial stress is felt; the same thermal expansion at a greater distance to the cylindrical axis has a lesser impact on stress than if it were closer.

4 Conclusions

A numerical model is presented which solves the steady-state temperature equation in cylindrical coordinates given mixed flux, convection and radiation boundary conditions. The temperature field is then used in the development of a Fourier expression for nonaxisymmetrical tube stress. The so-called Laplacian-Fourier $\mathscr{L}$-$\mathscr{F}$ Python model has been validated using an analytical case study for axisymmetrically heated tubes. An OpenFOAM® model was validated with the same case.

The $\mathscr{L}$-$\mathscr{F}$ Python model and OpenFOAM® model agree within reason in the estimation of linear-elastic thermal stress in long nonaxisymmetrically heated tubes. During the analysis it became apparent that the compressive axial component of stress is the most significant in the equivalent von Mises stress for this case. This component stress arises from the front-side to back-side temperature difference which, while having a zero net force in the axial direction, creates a bending moment in the tube's cross section.

Parameter studies revealed the inverse nature between tube internal convection coefficient and maximum tube thermal stress, that a little pressure can in fact decrease the impact of compressive axial thermal stress on the equivalent tube stress, that tube thermal stress is very sensitive to tube conductivity, and that large tube diameters lead to slightly lower thermal stress.

The advantage of the $\mathscr{L}$-$\mathscr{F}$ Python model is in its speed of calculation - 0.5 sec as opposed to hours in OpenFOAM®. It can be integrated with a 1D receiver flow model for better consideration of receiver fatigue in system or transient simulations, or in optimisation algorithms seeking to minimise tube stress as part of a larger model. The exploration of these options will build the body of ongoing work.

5 Acknowledgements

Many of the findings presented in this paper draws on research performed as part of the Australian Solar Thermal Research Initiative (ASTRI), a project supported by the Australian Government, through the Australian Renewable Energy Agency (ARENA). Responsibility for the views, information or advice expressed herein is not accepted by the Australian Government.

References

Coventry, J., Arjomandi, M., Asselineau, C.-A., Chinnici, A., Davis, D., Kim, J.-S., Kumar, A., Lipinski, W., Logie, W. R., Nathan, G., Pye, J. D., & Saw, W. 2016. Development of ASTRI high-temperature solar receivers. *In: 22nd Annual SolarPACES Conference*. Abu Dhabi.

Gatewood, B. E. 1941. Thermal stresses in long cylindrical bodies. *The London, Edinburgh, and Dublin Philosophical Magazine and Journal of Science*, **32**(213), 282–301.

Hetnarski, R. B., & Eslami, M. R. 2009. *Thermal Stress – Advanced Theory and Applications*. Springer.

Irfan, M. A., & Chapman, W. 2009. Thermal stresses in radiant tubes due to axial, circumferential and radial temperature distributions. *Applied Thermal Engineering*, **29**, 1913–1920.

Kim, J.-S., Potter, D., Gardner, W., Soo Too, Y. C., & Padilla, R. V. 2016. Ideal heat transfer conditions for tubular solar receivers with different design constraints. *In: 22nd Annual SolarPACES Conference*. Abu Dhabi.

Kiusalaas, J. 2010. *Numerical Methods in Engineering with Python*. 2nd edn. Cambridge University Press.

Liao, Z., Li, X., Xu, C., Chang, C., & Wang, Z. 2014. Allowable flux density on a solar central receiver. *Renewable Energy*, **62**, 747–753.

Logie, W. R., Asselineau, C.-A., Pye, J. D., & Coventry, J. 2015. Temperature and heat flux distributions in sodium receiver tubes. *In: Asia-Pacific Solar Research Conference*. Brisbane.

Marugán-Cruz, C., Flores, O., Santana, D., & García-Villalba, M. 2016. Heat transfer and thermal stresses in a circular tube with a non-uniform heat flux. *Int. J. Heat and Mass Transfer*, **96**, 256–266.

Pacheco, J. E., Ralph, M. E., Chavez, J. M., Dunklin, S. R., Rush, E. E., Ghanbari, C. M., & Matthews, M. W. 1995. *Results of molten salt panel and component experiments for solar central receivers: cold fill, freeze/thaw, thermal cycling and shock, and instrumentation*. Tech. rept. SAND94-2525. Sandia National Laboratories, Albuquerque.

Pye, J. D., Zheng, M., Zapata, J., Asselineau, C.-A., & Coventry, J. 2014. An exergy analysis of tubular solar-thermal receivers with different working fluids. *In: 20th Annual SolarPACES Symposium*. Beijing.

Timoshenko, S., & Goodier, J. N. 1951. *Theory of Elasticity*. McGraw-Hill Book Company, Inc.

Tuković, Z., Cardiff, P., Karač, A., Jasak, H., & Ivanković, A. 2014. OpenFOAM library for Fluid Structure Interaction. *In: 9th OpenFOAM Workshop*.

Winter, C. J., Sizmann, R. L., & Vant-Hull, L. L (eds). 1991. *Solar Power Plants*. Springer-Verlag.